The Astrophysical Journal Letters, 793:L12 (6pp), 2014 September 20 doi:10.1088/2041-8205/793/1/L12

A GEOMETRICALLY SUPPORTED $z \sim 10$ CANDIDATE MULTIPLY IMAGED BY THE HUBBLE FRONTIER FIELDS CLUSTER A2744

Adi Zitrin[1,14], Wei Zheng[2], Tom Broadhurst[3,4], John Moustakas[5], Daniel Lam[6], Xinwen Shu[7,8], Xingxing Huang[2,8], Jose M. Diego[9], Holland Ford[2], Jeremy Lim[6], Franz E. Bauer[10,11], Leopoldo Infante[10], Daniel D. Kelson[12], and Alberto Molino[13]
[1] Cahill Center for Astronomy and Astrophysics, California Institute of Technology, MS 249-17, Pasadena, CA 91125, USA; adizitrin@gmail.com
[2] Department of Physics and Astronomy, Johns Hopkins University, Baltimore, MD 21218, USA
[3] Department of Theoretical Physics, University of Basque Country UPV/EHU, Bilbao, Spain
[4] IKERBASQUE, Basque Foundation for Science, Bilbao, Spain
[5] Department of Physics and Astronomy, Siena College, Loudonville, NY 12211, USA
[6] Department of Physics, The University of Hong Kong, Pokfulam Road, Hong Kong
[7] CEA Saclay, DSM/Irfu/Service d'Astrophysique, Orme des Merisiers, F-91191 Gif-sur-Yvette Cedex, France
[8] Department of Astronomy, University of Science and Technology of China, Hefei, Anhui 230026, China
[9] Instituto de Física de Cantabria, CSIC-Universidad de Cantabria, E-39005 Santander, Spain
[10] Pontificia Universidad Católica de Chile, Instituto de Astrofísica, Santiago 22, Chile
[11] Space Science Institute, Boulder, CO 80301, USA
[12] The Observatories of the Carnegie Institution for Science, Pasadena, CA 91101, USA
[13] Instituto de Astrofísica de Andalucía - CSIC, Glorieta de la Astronomía, s/n. E-18008, Granada, Spain
Received 2014 July 14; accepted 2014 August 23; published 2014 September 4

ABSTRACT

The deflection angles of lensed sources increase with their distance behind a given lens. We utilize this geometric effect to corroborate the $z_{\rm phot} \simeq 9.8$ photometric redshift estimate of a faint near-IR dropout, triply imaged by the massive galaxy cluster A2744 in deep Hubble Frontier Fields images. The multiple images of this source follow the same symmetry as other nearby sets of multiple images that bracket the critical curves and have well-defined redshifts (up to $z_{\rm spec} \simeq 3.6$), but with larger deflection angles, indicating that this source must lie at a higher redshift. Similarly, our different parametric and non-parametric lens models all require this object be at $z \gtrsim 4$, with at least 95% confidence, thoroughly excluding the possibility of lower-redshift interlopers. To study the properties of this source, we correct the two brighter images for their magnifications, leading to a star formation rate of $\sim 0.3\ M_{\odot}\ {\rm yr}^{-1}$, a stellar mass of $\sim 4 \times 10^7\ M_{\odot}$, and an age of $\lesssim$220 Myr (95% confidence). The intrinsic apparent magnitude is 29.9 AB (F160W), and the rest-frame UV ($\sim$1500 Å) absolute magnitude is $M_{\rm UV,AB} = -17.6$. This corresponds to $\sim 0.1\ L^*_{z=8}$ ($\sim 0.2\ L^*_{z=10}$, adopting $dM^*/dz \sim 0.45$), making this candidate one of the least luminous galaxies discovered at $z \sim 10$.

Key words: galaxies: clusters: general – galaxies: clusters: individual (A2744) – galaxies: high-redshift – gravitational lensing: strong

Online-only material: color figures

1. INTRODUCTION

The Hubble Frontier Fields (HFF; Lotz et al. 2014; Coe et al. 2014) initiative is a *Hubble Space Telescope* (*HST*) Director's Discretionary Time program in which 4–6 massive galaxy clusters and parallel fields are being observed in the optical and near-infrared to an unprecedented depth (140 orbits; $m_{\rm AB,lim} \sim 29$). Coordinated observations with the *Spitzer Space Telescope* or other ground-base telescopes, and lens-map preparation by several groups, set the stage to advance our understanding of the early universe. This effort aims at reaching new frontiers of depth into high redshifts, so we may push beyond the current Hubble limit for faint field galaxies to better characterize the properties of the first galaxies and evaluate their role in (re)ionizing the intergalactic medium.

The HFF will achieve this goal by leveraging the strong gravitational lensing power of massive galaxy clusters, which deflect, distort, and—most importantly—magnify distant background galaxies. Thanks to this magnification, background objects that are intrinsically fainter than the observational threshold are magnified in flux and area, at fixed surface brightness, so that the detectability of small, poorly resolved objects is enhanced. Moreover, if the projected surface-mass density of the foreground lens is high enough, multiple images of the same background source often appear (see Bartelmann 2010; Kneib & Natarajan 2011, for reviews). For massive cluster lenses, many sets of multiple images are typically generated and can be used as constraints for constructing lens models, which can in turn be used to predict the lensing distance (ratio of the angular-diameter distances of the lens to the source, and the source, d_{ls}/d_s), and thus constrain the "geometric redshift" of other multiply imaged candidates. The critical curves are bound to expand, and deflection angles increase, with increasing source distance behind a given lens. This "nesting" effect (e.g., see related figures in Broadhurst et al. 2005; Zitrin et al. 2009; Lam et al. 2014) is especially useful for determining the lensing distance of high-redshift candidates that happen to be multiply imaged and for which spectroscopy is very challenging (e.g., Vanzella et al. 2011; Bradač et al. 2012; Finkelstein et al. 2013; Schenker et al. 2014).

The magnification by clusters of galaxies has consistently provided galaxies at the highest redshift limits (e.g., Franx et al. 1997; Frye et al. 2002; Stark et al. 2007; Bradley et al. 2008; Bouwens et al. 2012; Zheng et al. 2012). However, due to the small source-plane area at high redshifts, the chances of capturing a multiply imaged high-redshift galaxy are small,

[14] Hubble Fellow.

with only a few currently known (e.g., Franx et al. 1997; Kneib et al. 2004; Richard et al. 2011; Zitrin et al. 2012; Bradley et al. 2014; Monna et al. 2014; Atek et al. 2014; Zheng et al. 2014). The highest-redshift candidate to date was detected to be triply imaged at $z \sim 11$ (Coe et al. 2013). While the latter candidate seems secure in many aspects of its photometric redshift, including a scrutinizing comparison with colors of possible lower-z interlopers, the lens models could not unambiguously determine its redshift. Similarly, several other $z \sim 9$–11 objects are known from deep fields (e.g., Ellis et al. 2013; Bouwens et al. 2011, 2014; Oesch et al. 2013, 2014 and references therein), with redshifts estimated solely on basis of the photometry.

Here, we report a faint, geometrically supported candidate $z \sim 10$ galaxy, triply imaged by the HFF cluster Abell 2744 (A2744 hereafter). In Section 2, we summarize the relevant observations and photometry. In Section 3, we present the photometric redshifts, lens models, and results, which are discussed and summarized in Section 4. We assume a ΛCDM cosmology with $\Omega_M = 0.3$, $\Omega_\Lambda = 0.7$, and $H_0 = 100\,h$ km s^{-1} Mpc^{-1} with $h = 0.7$.

2. *HST* AND *SPITZER* OBSERVATIONS

HFF observations of A2744 ($z = 0.308$) were obtained between 2013 October 25 and 2014 July 1 as part of GO/DD 13495 (P.I.: Lotz). These data consist of 70 orbits with WFC3/IR in the F105W, F125W, F140W, and F160W near-infrared filters, and 70 orbits with ACS/WFC in the F435W, F606W, and F814W optical bandpasses. These observations were supplemented with archival ACS data, ∼13–16 ks in each of these optical filters, taken between 2009 October 27–30 (GO 11689, P.I.: Dupke). We also use one orbit imaging in each of the F105W and F125W bands, and 1.5 orbits in the F160W band, obtained in 2013 August and 2014 June–July (GO 13386; P.I.: Rodney).

A detailed description of our data reduction and photometry can be found in Zheng et al. (2014). Briefly, both the WFC3/IR and ACS images are processed using APLUS (Zheng 2012), an automated pipeline that originally grew out of the APSIS package (Blakeslee et al. 2003). We astrometrically align, resample, and combine all the available imaging in each filter to a common 0.″065 pixel scale, and create ultra-deep detection images from the inverse-variance weighted sum of the WFC3/IR and ACS images, respectively. The 5σ limiting magnitude in a 0.″4 diameter aperture in the final WFC3/IR images is approximately ∼29 AB, and ∼30 AB in the ACS optical mosaics.

Next, we run SExtractor (Bertin & Arnouts 1996) in dual-image mode using the WFC3/IR image stack as the detection image. We require sources to be detected with a minimum signal-to-noise ratio of 1.5 spanning at least four connected pixels. We measure colors using an isophotal aperture defined in the detection image, which balances the need between depth and photometric precision (Ferguson & McGaugh 1995). Finally, we identify high-redshift galaxy candidates by looking for a strong Lyman break using the color cuts given in Zheng et al. (2014), supplemented by careful visual inspection. For sources of interest lying near cluster members, such as JD1B and JD1C here (see below), we first run GALFIT (Peng et al. 2010) to remove the nearby members, before running SExtractor. Similarly, for JD1A, a nearby star was removed prior to the photometry (see Section 3).

In addition to the *HST* observations, we also utilize *Spitzer*/IRAC imaging of A2744 obtained as part of Program 90257 (P.I.: Soifer) between 2013 September and 2014 February, supplemented with archival imaging from 2004 (Program 84; P.I.: Rieke). We process the IRAC Basic Calibrated Data (cBCD) images using standard methods implemented in MOPEX (Makovoz & Khan 2005), and create a final mosaic in each channel with a pixel scale of 0.″6. The total exposure time of the final mosaics is ∼340 ks, achieving a 1σ limiting magnitude of 27.3 in channel 1 (IRAC1, 3.6 μm) and 27.1 in channel 2 (IRAC2, 4.5 μm). More details on the IRAC photometry will be given in X. Huang et al. (in preparation).

3. DISCOVERY OF THE $z \sim 10$ CANDIDATE

We initially identified our high-redshift galaxy candidate as a *J*-band dropout near the center of A2744 (hereafter JD1A). A preliminary estimate of JD1A's photometric redshift (see below) suggested it was most likely at $z \sim 10$, although there was a non-negligible probability of it being a lower-redshift ($z \sim 2$–3) interloper.

In order to assess these two possibilities, and motivated by the vicinity to the critical curves, we use an updated version of our publicly available light traces mass (LTM) gravitational lensing model of A2744.[15] The LTM model assumes that both the baryonic and dark matter mass distributions can be traced by the cluster's light distribution (Broadhurst et al. 2005), where the latter mass component is a smoothed version of the former. This method has been most successful at uncovering large numbers of multiply imaged galaxies in many galaxy clusters (e.g., Zitrin et al. 2009, 2013), including A2744 (Merten et al. 2009). Compared to the publicly accessible LTM model of A2744, our new LTM model uses the updated catalog of multiple images from Lam et al. (2014 and references therein), spanning the redshift range $z \sim 1$–7 (Atek et al. 2014; Zheng et al. 2014). In Figure 1, we show a color mosaic of the central region of A2744 together with the critical curves at several different source redshifts based on our updated LTM model, and the multiple-image constraints from Lam et al. (2014).

Using our LTM model, we de-lens JD1A to the source-plane and back, considering both the low- and high-redshift hypotheses. A source redshift of $z \sim 2$ predicts a counter-image ∼3″ northeast of the position of JD1A, and a second counter-image approximately 20″ west of the southern core of the cluster; however, no other objects are located at either of these predicted positions within ∼1″–2″ (the image reproduction precision rms of our model is ∼1.″3). A source redshift of $z \sim 10$, on the other hand, yields the same positional symmetry of multiple images as in the $z \sim 2$ case, but—as expected—with larger deflection angles. Remarkably, we find faint *J*-band dropout galaxies near both predicted counter-image locations (Figure 1): image B (hereafter JD1B), and, on the other side of the cluster, a significantly fainter image C (hereafter, JD1C), although note that this identification is tentative due to this object's faintness.

We use several independent lensing models to verify the positions of the predicted multiple images. First, we construct a second model with the updated Zitrin et al. (2009) pipeline, which adopts the LTM assumption only for the galaxies, yet follows an analytical form for the dark matter, namely (projected), elliptical NFW distributions (eNFW; Navarro et al. 1996) for the main mass clumps (see Zitrin et al. 2013). This model (hereafter "NFW") is basically identical to the ZITRIN NFW model

[15] For details regarding the HFF lens models, see http://archive.stsci.edu/prepds/frontier/lensmodels.

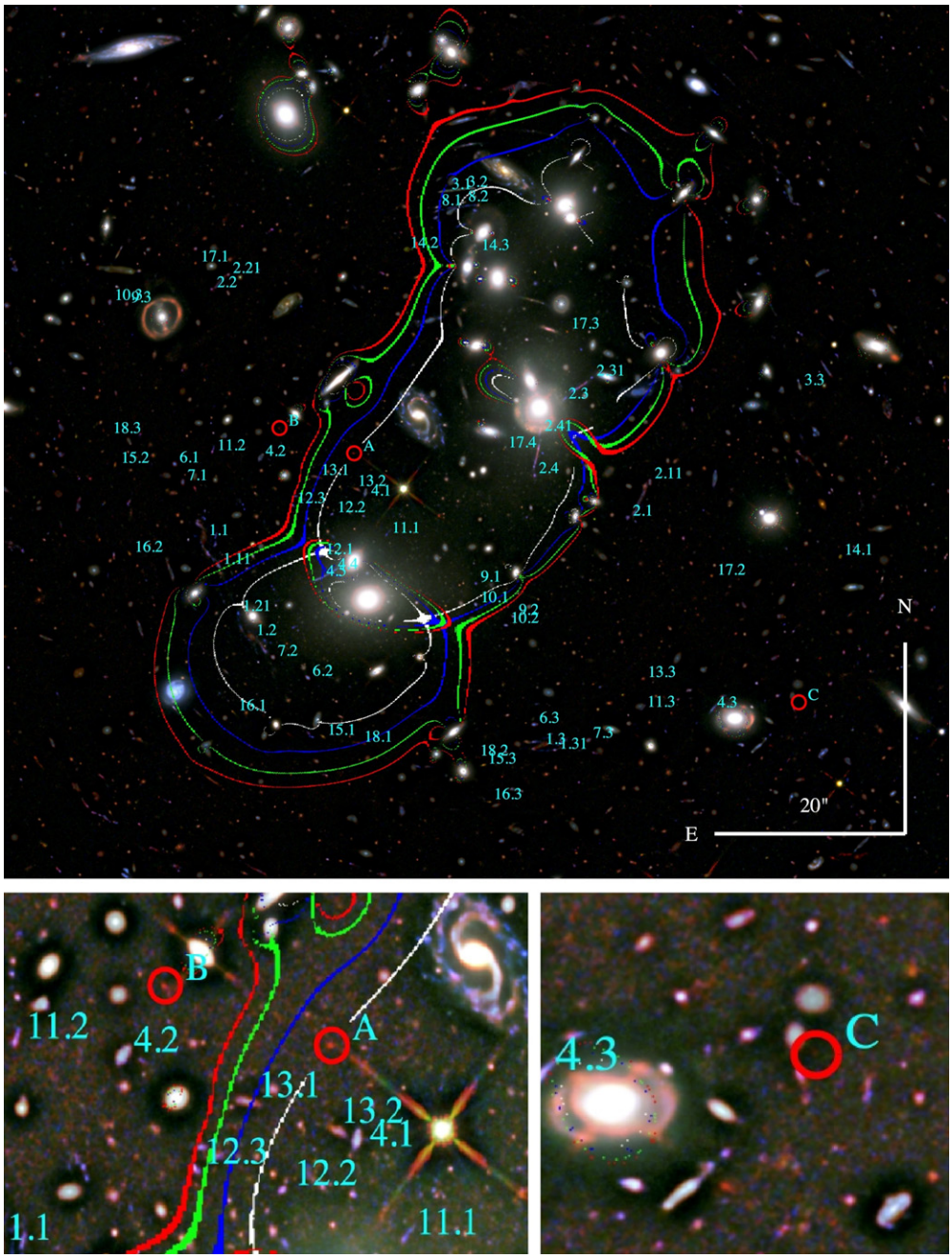

Figure 1. Smoothed color mosaic of A2744 (R = F160W+F140W; G = F125W+F105W+F814W; B = F606W+F435W) with the expanding critical curves for increasing source redshifts (white: $z_s \simeq 1.3$ (system 13); blue: $z_s \simeq 2$; green: $z_s \simeq 3.6$ (system 4, Richard et al. 2014); red: $z_s \sim 10$) based on our LTM lens model overlaid. The numbered labels indicate the multiple images from Lam et al. (2014) used as constraints, and the *red* circles mark the three images (A, B, and C) of our candidate $z \sim 10$ dropout galaxy. Our models completely exclude $z \sim 2$–3 lower redshifts as a possible solution for this system, as the critical curves should pass midway between the two mirrored images, e.g., A and B here, seen better in the bottom left panel. The bottom right panel similarly shows a zoom-in on our best identification for the least magnified image of this system, image C.

(A color version of this figure is available in the online journal.)

released as part of the HFF, but has been updated using the Lam et al. (2014) multiple-image catalog. Finally, we also check our results against the lensing model of A2744 supplied by the CATS team (e.g., Richard et al. 2014), constructed using the parametric Lenstool algorithm (Jullo et al. 2007), and against the free-form lensing model published by Lam et al. (2014), which combines both parametric and non-parametric techniques.

We find that all four lensing models yield consistent results regarding the predicted multiple image positions of JD1. Quantitatively, our LTM model yields $z \gtrsim 4$ for our candidate, while our "NFW" model requires $z \gtrsim 8$, both with 95% confidence based on more than 10,000 Markov Chain Monte-Carlo steps. The Lam et al. (2014) and Lenstool models, respectively, yield similar results. To illustrate this result, in Figure 2, we use the Lam et al. (2014) model to plot the predicted positions of images A, B, and C as a function of source redshift in the range $z = 2$–12. This analysis shows that a high-redshift solution for our candidate is clearly favored over the lower-redshift ($z \sim 2$–3) alternative.

Our LTM model implies magnifications of $10.01^{+1.1}_{-0.86}$, $11.25^{+4.8}_{-2.5}$, and $3.57^{+0.33}_{-0.03}$ (95% confidence intervals) for JD1A, JD1B, and JD1C, respectively (Table 1). These values are

Table 1
Photometry, Redshifts, and Magnifications of Our $z \sim 10$ Candidate

Name	R.A. (J2000, deg)	Decl. (J2000, deg)	F160W (nJy)	F140W (nJy)	F125W (nJy)	F105W (nJy)	F814W (nJy)	3.6 μm[a] (nJy)	4.5 μm[a] (nJy)	μ_{LTM}[b]	iSEDfit Redshift[c]	BPZ Redshift[c]
JD1A	3.59251	−30.40149	35.4 ± 1.4	21.8 ± 1.7	12.7 ± 1.4	1.2 ± 1.1	4.3 ± 2.2	<91	<80	$10.01^{+1.1}_{-0.86}$	$9.59^{+0.51}_{-7.11}$	$9.72^{+0.16}_{-7.60}$
JD1B	3.59502	−30.40075	43.8 ± 2.9	24.3 ± 2.5	14.4 ± 2.0	2.0 ± 1.3	2.1 ± 3.7	<82	<67	$11.25^{+4.8}_{-2.5}$	$9.66^{+0.81}_{-7.32}$	$9.83^{+0.22}_{-0.44}$
JD1C	3.57753	−30.40871	10.7 ± 0.7	3.9 ± 1.3	0.7 ± 1.2	-2.0 ± 2.4	1.7 ± 0.7	<105	<141	$3.57^{+0.33}_{-0.03}$	$10.95^{+0.93}_{-9.51}$	$11.09^{+0.68}_{-0.97}$
Total[d]	...	...	89.9 ± 3.3	50.0 ± 3.3	27.8 ± 3.1	1.2 ± 2.9	8.1 ± 4.4	<161	<175	...	$9.80^{+0.44}_{-7.10}$	$9.83^{+0.16}_{-0.30}$

Notes.
[a] Local limiting fluxes ($\sim 1\sigma$ upper limits) estimated by running GALFIT to model the IRAC images in a $\sim 13'' \times 13''$ region around each position to subtract all nearby sources, and measuring the rms fluctuation of the residual images.
[b] Magnifications and 95% confidence intervals from our LTM gravitational lensing model.
[c] Uncertainties on the photometric redshifts are 95% confidence intervals.
[d] Summed flux of all three sources (JD1A+JD1B+JD1C) with the uncertainties added in quadrature.

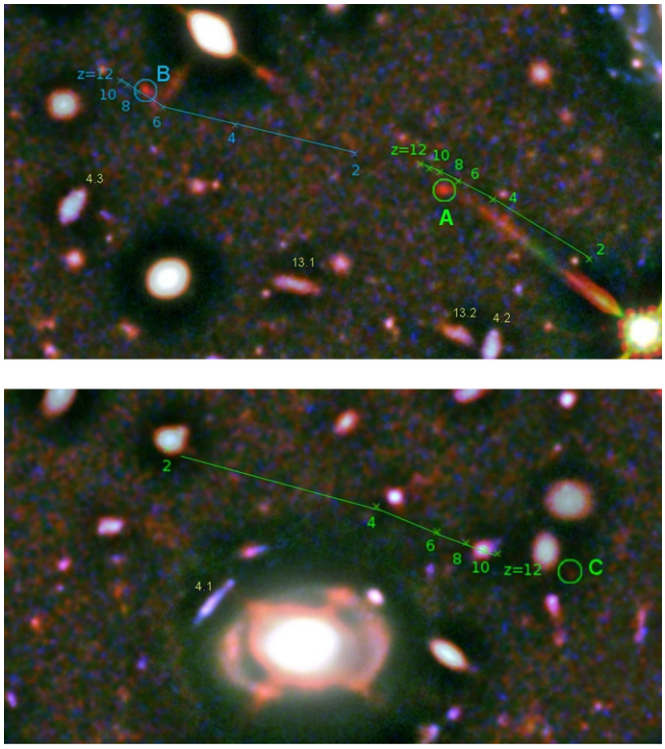

Figure 2. Top: Loci of predicted positions for images A and B using the Lam et al. (2014) model. Images A and B lie close to two other pairs of multiply imaged galaxies at lower redshifts, systems 4 and 13, which also bracket the tangential critical curve (Figure 1). The blue track corresponds to the predicted image position of B using the observed location of image A, and the green track shows the opposite. The predictions are shown over a wide redshift range $2 < z < 12$. High redshift is clearly preferred, explicitly $z > 6$, but note that the predicted positions converge at high redshift because of the saturation of the lensing-distance relation (so that a range of high-redshift solutions is allowed). Low redshifts, however, are very clearly excluded. Bottom: similar prediction pattern for image C, again showing the high-z preference.
(A color version of this figure is available in the online journal.)

broadly consistent with the magnifications predicted by our updated "NFW" model, and with the magnifications inferred using the Lenstool and Lam et al. (2014) lensing models, although these can reach up to ~ 2 times higher magnifications for images A and B, and $\sim 50\%$ lower magnification for image C, and the reader should refer to these as the typical systematic uncertainties here. For calculating the source properties, we shall use the magnifications from our LTM model, which renders our calculation conservative in the sense that higher magnifications for A and B yield an even smaller and fainter source than inferred in Section 4.

In Figure 3, we show $1\farcs74 \times 1\farcs74$ postage stamp cutouts of JD1A, JD1B, and JD1C in the observed-frame optical and near-infrared. JD1A and JD1B are clearly detected in the three reddest bands (F125W, F140W, and F160W), but vanish in the F105W bandpass and blueward, suggesting that we are observing the Lyman break at $z \sim 9$–10. JD1C is significantly fainter, but also appears to have a Lyman break at the same observed-frame wavelength.

We quantify these results in Figure 4, where we show the spectral energy distributions (SEDs) and photometric redshift probability distributions of all three sources, as well as the sum (JD1A + JD1B + JD1C). We compute photometric redshifts using two independent codes: iSEDfit (Moustakas et al. 2013) and BPZ (Bayesian Photometric Redshifts; Benítez 2000; Coe et al. 2006). BPZ relies on a suite of 11 galaxy templates that have been carefully calibrated using spectroscopic samples over a wide range of redshift and apparent magnitude. Like BPZ, iSEDfit is also a Bayesian SED-modeling code, but one that uses stellar population synthesis models to infer the photometric redshifts and physical properties of galaxies. Using iSEDfit, we construct a Monte Carlo grid of 20,000 models spanning a wide range of star formation history, age, stellar metallicity, dust content, and nebular emission-line strength (see Zheng et al. 2014 for details).

Both BPZ and iSEDfit indicate high-redshift solutions for both JD1A and JD1B, $z_{\rm phot} \simeq 9.6$–9.8, with a secondary small peak at $z_{\rm phot} \sim 2.5$. For JD1C, the preferred redshift is $z_{\rm phot} \simeq 11$, with a secondary solution at $z_{\rm phot} \simeq 2.5$, although iSEDfit finds a flatter redshift probability distribution allowing less-likely solutions throughout the full redshift range. Given the faintness of JD1C compared to the other two images, and with the supporting evidence from our lensing analysis, we are confident that JD1 is indeed at $z_{\rm phot} \simeq 9.8$.

We conclude this section by describing some additional tests we have carried out to check the fidelity of our high-redshift candidate. First, we verify that all three images of our candidate are also present in the publicly distributed HFF image mosaics, which are independently processed using the MosaicDrizzle pipeline (Koekemoer et al. 2011).[16] Second, we check the possibility that JD1A may be an artifact of the nearby stellar diffraction spike (see Figure 1, although we note that even by eye JD1A is clearly offset from the diffraction trail). We select a comparably bright, isolated star elsewhere in the F160W mosaic

[16] http://www.stsci.edu/hst/campaigns/frontier-fields/FF-Data

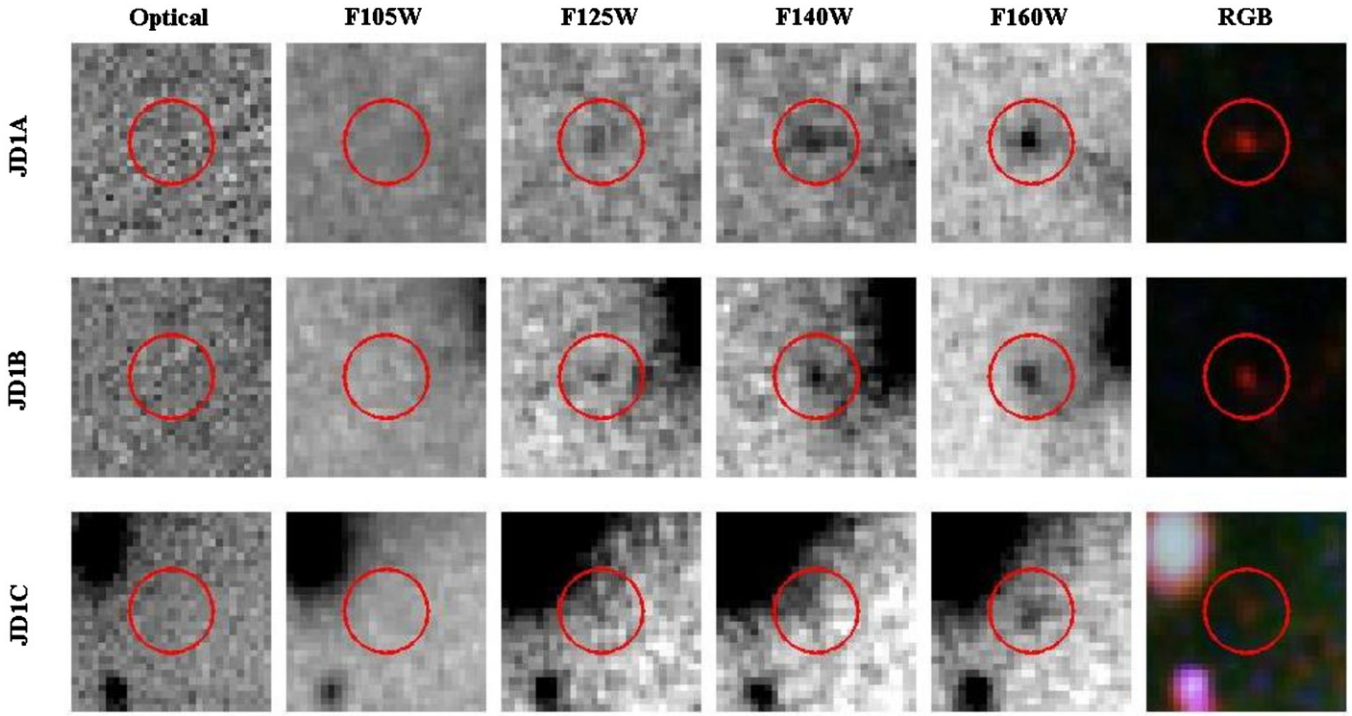

Figure 3. Image cutouts of the three multiple images of our $z \sim 10$ candidate, showing the vanishing flux blueward of the $J_{\rm F125W}$ band.
(A color version of this figure is available in the online journal.)

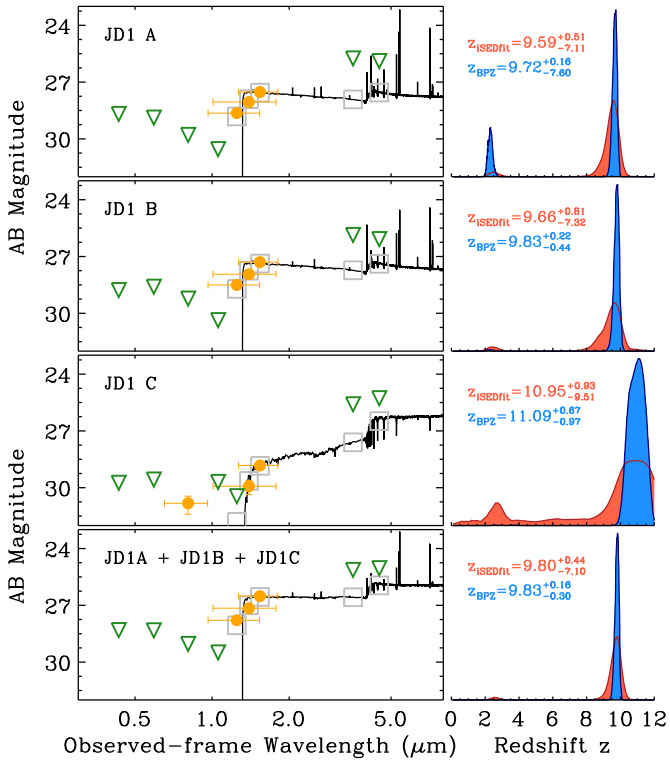

Figure 4. Left: observed-frame spectral energy distribution (SED) of JD1A, JD1B, JD1C, and of the sum of all three images, JD1A+JD1B+JD1C. The orange points represent statistically significant detections, the green triangles are 2σ upper limits, the black spectrum shows the best-fitting (maximum likelihood) model fit from `iSEDfit`, and the open gray squares represent the best-fitting SED convolved with the *HST* filter response curves. Right: photometric redshift probability distribution for each observed SED based on both `iSEDfit` (red shading) and `BPZ` (blue shading). The legend indicates the redshift at the maximum of the marginalized posterior probability distribution, and the 95% confidence intervals, inferred using each code.
(A color version of this figure is available in the online journal.)

and use its cutout to subtract (after centering and rescaling) the star near JD1A. Because the diffraction spikes in the mosaic are all aligned, this procedure effectively subtracts the offending star and leaves JD1A unaffected, indicating that it is not an artifact (note that the photometry for JD1A was performed on these star-subtracted images). As an additional check, we also inspect the archival WFC3/IR imaging of A2744 from GO 13386 (P.I.: Rodney), which is rotated by approximately 9° relative to the HFF mosaics, and find that both JD1A and JD1B are present (although only within the noise level due to the shallowness of this imaging), again suggesting these are not artifacts related to the spikes. Finally, we verify that neither JD1A nor JD1B are moving foreground objects by creating custom mosaics from the first and second half of the individual F160W exposures obtained as part of the HFF observations. JD1A and JD1B are both clearly detected in both mosaics. Furthermore, subtracting the two mosaics causes both sources to disappear, again indicating that these are bona fide extragalactic sources.

4. DISCUSSION AND CONCLUSIONS

We report the discovery of a $z \sim 10$ Lyman break galaxy multiply imaged by the massive galaxy cluster A2744, which has been observed to an unprecedented depth with *HST* as part of the HFF campaign. This candidate adds to just several other galaxies reported to be at $z \sim 9$–11 (see Section 1), and therefore provides important insight into galaxy formation at the earliest epochs. Despite the lack of spectroscopy for such high-redshift objects, with a variety of well-constrained lens models we are able to geometrically confirm that this object must lie at high redshift.

To constrain the physical properties of our candidate, we fix the redshift at the most probable redshift, $z_{\rm phot} = 9.8$, and use `iSEDfit` to construct a large suite of model SEDs. After accounting for the individual magnifications of each image (see

Table 1), we find that JD1 has a stellar mass of $\sim 4 \times 10^7\ M_\odot$ and is forming stars at approximately 0.3 $M_\odot\ \mathrm{yr}^{-1}$, implying a doubling time[17] of ∼500 Myr, comparable to the age of the universe at $z = 9.8$. Using the two brightest sources (JD1A and JD1B), we are also able to constrain the star formation rate-weighted age to <220 Myr (95% confidence), implying a formation redshift of $z_f < 15$.

To examine the intrinsic size of the galaxy, we focus on JD1A. We measure an approximate half-light radius of ∼0.″1 in the image plane, corresponding to a de-lensed half-light radius of $\lesssim$0.″03 ($\lesssim$0.13 kpc). This source size is several times smaller than expected following recent $z \sim 9$–10 candidates uncovered in deep fields (e.g., Ono et al. 2013; Oesch et al. 2014; Holwerda et al. 2014), or, following the observed size evolution extrapolated from lower redshifts (Coe et al. 2013 and references therein). However, the source size we find matches very well the size of the lensed $z \simeq 10.7$ candidate galaxy published by Coe et al., who showed that although being smaller than expected by a factor of a few, the typical factor of ∼2 scatter in size found in somewhat lower-redshift galaxies alleviates the discrepancy. It is interesting that both of these highest-redshift multiply imaged candidates to date exhibit smaller sizes than high-z field objects.

Finally, the magnification by our lens models indicate that the intrinsic apparent magnitude is 29.9 AB (F160W), and the rest-frame UV (∼1500 Å) absolute magnitude is $M_{\mathrm{UV,AB}} = -17.6$, corresponding to $\sim 0.1\ L^*_{z=8}$, or $\sim 0.2\ L^*_{z=10}$ (extrapolated with $dM^*/dz \sim 0.45$). This makes this galaxy one of the least luminous $z \sim 10$ candidates ever discovered, supplying a first taste of the upcoming achievements of the HFF observational effort—reaching deeper into the faint end of the high-redshift luminosity function.

We kindly thank the anonymous reviewer of this work for useful comments. Useful discussions with Rychard Bouwens, Richard Ellis, and Larry Bradley are much appreciated. This work is based on observations made with the NASA/ESA *Hubble Space Telescope* and was supported by award AR-13079 from the Space Telescope Science Institute (STScI), which is operated by the Association of Universities for Research in Astronomy, Inc. under NASA contract NAS 5-26555. It is also based on observations from the *Spitzer Space Telescope*, which is operated by the Jet Propulsion Laboratory, California Institute of Technology under a contract with NASA. This work utilizes gravitational lensing models produced by P.I.s Zitrin and Merten, and P.I. Ebeling, funded as part of the HST Frontier Fields program conducted by STScI. Support for this work was provided by NASA through Hubble Fellowship grant #HST-HF-51334.01-A awarded by STScI.

[17] The time it would take for the galaxy to double its stellar mass, assuming a 25% gas loss factor appropriate for a ∼200 Myr stellar population (Behroozi et al. 2013).

REFERENCES

Atek, H., Richard, J., Kneib, J.-P., et al. 2014, ApJ, 786, 60
Bartelmann, M. 2010, CQGra, 27, 233001
Behroozi, P. S., Wechsler, R. H., & Conroy, C. 2013, ApJ, 770, 57
Benítez, N. 2000, ApJ, 536, 571
Bertin, E., & Arnouts, S. 1996, A&AS, 117, 393
Blakeslee, J. P., Anderson, K. R., Meurer, G. R., Benítez, N., & Magee, D. 2003, in ASP Conf. Ser. 295, Astronomical Data Analysis Software and Systems XII, ed. H. E. Payne, R. I. Jedrzejewski, & R. N. Hook (San Francisco, CA: ASP), 257
Bouwens, R., Bradley, L., Zitrin, A., et al. 2012, arXiv:1211.2230
Bouwens, R. J., Illingworth, G. D., Labbe, I., et al. 2011, Natur, 469, 504
Bouwens, R. J., Illingworth, G. D., Oesch, P. A., et al. 2014, arXiv:1403.4295
Bradač, M., Vanzella, E., Hall, N., et al. 2012, ApJL, 755, L7
Bradley, L. D., Bouwens, R. J., Ford, H. C., et al. 2008, ApJ, 678, 647
Bradley, L. D., Zitrin, A., Coe, D., et al. 2014, ApJ, 792, 76
Broadhurst, T., Benítez, N., Coe, D., et al. 2005, ApJ, 621, 53
Coe, D., Benítez, N., Sánchez, S. F., et al. 2006, AJ, 132, 926
Coe, D., Bradley, L., & Zitrin, A. 2014, arXiv:1405.0011
Coe, D., Zitrin, A., Carrasco, M., et al. 2013, ApJ, 762, 32
Ellis, R. S., McLure, R. J., Dunlop, J. S., et al. 2013, ApJL, 763, L7
Ferguson, H. C., & McGaugh, S. S. 1995, ApJ, 440, 470
Finkelstein, S. L., Papovich, C., Dickinson, M., et al. 2013, Natur, 502, 524
Franx, M., Illingworth, G. D., Kelson, D. D., van Dokkum, P. G., & Tran, K.-V. 1997, ApJL, 486, L75
Frye, B., Broadhurst, T., & Benítez, N. 2002, ApJ, 568, 558
Holwerda, B. W., Bouwens, R., Oesch, P., et al. 2014, arXiv:1406.1180
Jullo, E., Kneib, J.-P., Limousin, M., et al. 2007, NJPh, 9, 447
Kneib, J.-P., Ellis, R. S., Santos, M. R., & Richard, J. 2004, ApJ, 607, 697
Kneib, J.-P., & Natarajan, P. 2011, A&ARv, 19, 47
Koekemoer, A. M., Faber, S. M., Ferguson, H. C., et al. 2011, ApJS, 197, 36
Lam, D., Broadhurst, T., Diego, J. M., et al. 2014, arXiv:1406.2702
Lotz, J., Mountain, M., Grogin, N. A., et al. 2014, in American Astronomical Society Meeting Abstracts, Vol. 223, American Astronomical Society Meeting Abstracts, #254.01
Makovoz, D., & Khan, I. 2005, in ASP Conf. Ser. 347, Astronomical Data Analysis Software and Systems XIV, ed. P. Shopbell, M. Britton, & R. Ebert (San Francisco, CA: ASP), 81
Merten, J., Cacciato, M., Meneghetti, M., Mignone, C., & Bartelmann, M. 2009, A&A, 500, 681
Monna, A., Seitz, S., Greisel, N., et al. 2014, MNRAS, 438, 1417
Moustakas, J., Coil, A. L., Aird, J., et al. 2013, ApJ, 767, 50
Navarro, J. F., Frenk, C. S., & White, S. D. M. 1996, ApJ, 462, 563
Oesch, P. A., Bouwens, R. J., Illingworth, G. D., et al. 2013, ApJ, 773, 75
Oesch, P. A., Bouwens, R. J., Illingworth, G. D., et al. 2014, ApJ, 786, 108
Ono, Y., Ouchi, M., Curtis-Lake, E., et al. 2013, ApJ, 777, 155
Peng, C. Y., Ho, L. C., Impey, C. D., & Rix, H.-W. 2010, AJ, 139, 2097
Richard, J., Jauzac, M., Limousin, M., et al. 2014, MNRAS, 444, 268
Richard, J., Kneib, J.-P., Ebeling, H., et al. 2011, MNRAS, 414, L31
Schenker, M. A., Ellis, R. S., Konidaris, N. P., & Stark, D. P. 2014, arXiv:1404.4632
Stark, D. P., Ellis, R. S., Richard, J., et al. 2007, ApJ, 663, 10
Vanzella, E., Pentericci, L., Fontana, A., et al. 2011, ApJL, 730, L35
Zheng, W. 2012, in Seventh Conference on Astronomical Data Analysis, ed. J.-L. Starck & C. Surace (Cargése: ADA), ada7.cosmostat.org/proceedings.php
Zheng, W., Postman, M., Zitrin, A., et al. 2012, Natur, 489, 406
Zheng, W., Shu, X., Moustakas, J., et al. 2014, arXiv:1402.6743
Zitrin, A., Broadhurst, T., Umetsu, K., et al. 2009, MNRAS, 396, 1985
Zitrin, A., Meneghetti, M., Umetsu, K., et al. 2013, ApJL, 762, L30
Zitrin, A., Moustakas, J., Bradley, L., et al. 2012, ApJL, 747, L9